



Flexible filaments buckle into helicoidal shapes in strong compressional flows

Brato Chakrabarti¹, Yanan Liu²✉, John LaGrone¹, Ricardo Cortez³, Lisa Fauci¹, Olivia du Roure¹, David Saintillan¹✉ and Anke Lindner¹

The occurrence of coiled or helical morphologies is common in nature, from plant roots to DNA packaging into viral capsids, as well as in applications such as oil drilling processes. In many examples, chiral structures result from the buckling of a straight fibre either with intrinsic twist or to which end moments have been applied in addition to compression forces. Here, we elucidate a generic way to form regular helicoidal shapes from achiral straight filaments transported in viscous flows with free ends. Through a combination of experiments using fluorescently labelled actin filaments in microfluidic divergent flows and two distinct sets of numerical simulations, we demonstrate the robustness of helix formation. A nonlinear stability analysis is performed, and explains the emergence of such chiral structures from the nonlinear interaction of perpendicular planar buckling modes, an effect that solely requires a strong compressional flow, independent of the exact nature of the fibre or type of flow field. The fundamental mechanism for the uncovered morphological transition and characterization of the emerging conformations advance our understanding of several biological and industrial processes and can also be exploited for the controlled microfabrication of chiral objects.

The interaction of flexible structures with viscous flows is central for a wide range of important biological and industrial processes, such as the swimming of flagellated microorganisms¹, the squeezing of red blood cells through microcapillaries², mitotic spindle formation and positioning during cell division³ or the design of soft micromechanical sensors⁴. In all cases, the dynamics and morphologies of the flexible objects subject to viscous stresses underlie the observed or desired properties.

Particularly rich dynamics occur when flexible objects are elongated⁵, where complex morphologies emerge as non-uniform viscous stresses overcome structural rigidity. Elongated shapes not only lead to drag anisotropy but also result in high deformability, as bending rigidity is strongly dependent on geometry in addition to material properties. Buckling instabilities of freely transported flexible fibres have been predicted, simulated and experimentally observed in shear as well as stagnation point flows^{6–10} and result in characteristic two-dimensional (2D) buckling modes. Under sedimentation, flexible fibres spontaneously adopt a steady U shape, independent of initial conditions¹¹. Flexible filaments can also be compressed into more compact, three-dimensional (3D) conformations under stronger forcing, and fibre coiling from the ends has been reported in shear^{12–16}. However, these morphologies are typically irregular and random, except for very specific initial conditions, where, for instance, knot formation has been observed¹⁷.

Here, we report on the surprising finding that a freely suspended straight flexible filament can buckle into a helical shape in a purely compressional flow. The formation of such regular 3D conformations^{18–21} typically requires applying end moments in addition to compressive forces^{22–24}. The phenomenon discussed here thus stands out from classical helical buckling in that the filament spontaneously adopts a chiral helicoidal morphology in the absence of any intrinsic twist or external moments.

We elucidate this generic morphological transition through a combination of experiments, simulations and theoretical modelling. To induce and visualize buckling in experiments, we passed fluorescently labelled actin filaments through a convergent–divergent hyperbolic microfluidic channel specially designed and optimized to provide uniform extension and compression rates over large distances while ensuring a long residence time for the filaments^{25,26}. These experiments are complemented by two sets of very different simulations. In the first model, closely mimicking the experimental conditions, we performed Langevin simulations of inextensible Euler–Bernoulli beams placed in a 2D flow field and subject to thermal fluctuations¹⁴. In the second model, we simulated non-Brownian elastic fibres composed of surface nodes connected by a network of springs providing structural rigidity and bending resistance^{15,27} in an axisymmetric channel¹⁶. As shown below, both types of simulation, as well as seminal simulations by Chelakkot et al.²⁸, recapitulate the helix formation seen in experiments, pointing to a very generic transition that only requires a strong compressional flow as we rationalize below using a nonlinear stability analysis. Our findings highlight a new mechanism by which a one-dimensional (1D) object can buckle into a chiral helicoidal shape under viscous loading. This mechanism remained undiscovered as typical experimental setups in stagnation point flows do not allow for sufficiently strong compression rates or long residence times, and as past theoretical analyses have been limited to two dimensions. Our results also underscore the robustness of this phenomenon, which occurs independent of the presence of thermal fluctuations and across very different flow environments.

Strong compressional flows induce helical buckling

Typical buckling events in experiments and Brownian simulations are shown in Fig. 1a for increasing values of the dimensionless elastoviscous number $\bar{\mu}$ (ref. ⁵), a measure of compression rate whose

¹Department of Mechanical and Aerospace Engineering, University of California San Diego, La Jolla, CA, USA. ²Laboratoire de Physique et Mécanique des Milieux Hétérogènes, UMR 7636, ESPCI Paris, PSL Research University, CNRS, Université Paris Diderot, Sorbonne Université, Paris, France. ³Department of Mathematics, Tulane University, New Orleans, LA, USA. ✉e-mail: yanan.liu@nwu.edu.cn; dstn@ucsd.edu

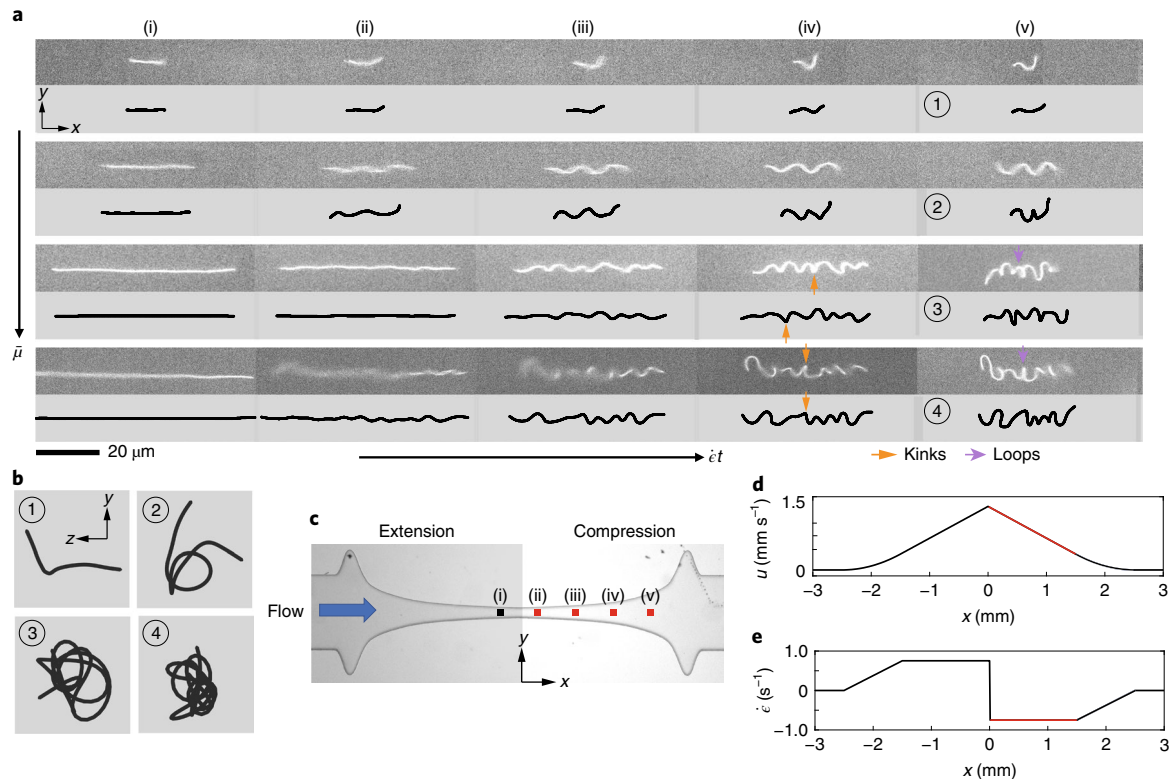


Fig. 1 | Buckling conformations of Brownian filaments in compressional flow. **a**, Snapshots of evolving filament morphologies from experiments and Brownian simulations compared at the same \dot{t} , measured from the instant the filament enters the compressional region. Vertical panels correspond to increasing values of $\bar{\mu}$. The filament is initially extended and aligned with the centreline (i), and it starts buckling after experiencing compression. For sufficiently large $\bar{\mu}$, 3D shapes emerge, as evidenced by kinks and loops in the 2D projections. Also see Supplementary Videos 1–5. Parameter values (from top to bottom): $l_p/L = 1.5, 0.76, 0.32, 0.25$; $\bar{\mu} = 2 \times 10^3, 3 \times 10^4, 8 \times 10^5, 2 \times 10^6$. **b**, Projections of simulated filament conformations corresponding to **a**(v) in the cross-sectional plane of the channel, highlighting the 3D helicoidal nature of the morphologies at large $\bar{\mu}$. **c**, Geometry of the optimized hyperbolic microfluidic channel used in experiments, with markers indicating the positions where the snapshots shown in **a** were taken. **d,e**, Axial velocity u and $\dot{\epsilon}$ as functions of streamwise position x along the channel centreline where filaments are transported. A constant $\dot{\epsilon}$ occurs over a given distance, and measurements are made in the compressional region highlighted in red.

definition we specify below. We focus here on the dynamics in the divergent part of a microfluidic hyperbolic channel (see Fig. 1c–e) where compression at constant strain rate $\dot{\epsilon}$ occurs, with the convergent part mainly serving to align and prestretch the filaments before measurements begin. As the filaments enter the compressional region (column (i)), they are indeed mostly straight, as thermal shape fluctuations have been largely suppressed⁸. Snapshots at increasing values of the dimensionless time \dot{t} in columns (ii) to (v) show the growth of deformations with distinct emergent morphologies for increasing elastoviscous numbers (top to bottom). In relatively weak flows (first row), deformations are mostly planar and resemble those seen in past studies in stagnation point flows^{8,29,30}. As $\bar{\mu}$ is increased in subsequent rows, more complex shapes emerge that are fully 3D, as evidenced by the blurriness of some parts of the filaments in the experimental images due to deformations out of the focal plane. Another indicator of three-dimensionality is the presence of apparent kinks (orange arrows) in the 2D images, which must result from the projection of 3D shapes. In some cases, actual loops (purple arrows) can be observed and strongly hint at helicoidal shapes. This is confirmed in Fig. 1b, showing simulated Brownian filament projections in the cross-sectional plane, where these loops are now clearly visible. The number of loops along the filament increases with $\bar{\mu}$ as higher unstable buckling modes become excited. The emerging coiled structures have no preferred chirality as expected from symmetry; this was tested in Brownian simulations, where simulations at a fixed $\bar{\mu}$ produce shapes of the

two chiralities with equal probability. In some cases, reversals in the handedness also occur at topological perversions along the contour length. As experimental observations only provide 2D projections, we cannot conclude on the chirality of the emerging 3D shapes. However, helices with perversions are also observed, leading us to believe that the conclusions from the Brownian simulations also hold in experiments and that there is no signature of the intrinsic chirality of the actin filaments in the 3D shapes. As the filament is transported downstream, the helix is further compressed by the flow until it exits the compressional region and is finally allowed to relax.

Simulations of a non-Brownian fibre in Fig. 2 are consistent with these observations and provide a cleaner picture of the buckling process. In the absence of thermal fluctuations, deformations are typically concentrated near the centre of the filament, with the filament ends remaining mostly straight and aligned with the flow axis. In simulations at moderate flow strengths, we find that deformations first occur in a 2D plane before 3D effects kick in and lead to the helix formation. This curious sequence of events, which we elucidate below, disappears in very strong flows, where 3D shapes emerge almost instantly. As in the Brownian case, shape perversions occasionally arise along the filament and cause handedness reversals^{22,31}.

Helical shapes stem from interacting planar modes

We proceed to explain the emergence of helical morphologies using a 3D weakly nonlinear stability analysis. Previous 2D linear analyses in planar flows have been very successful at predicting the onset

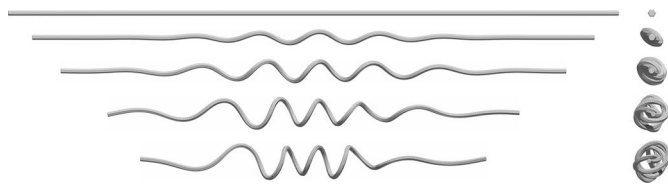


Fig. 2 | Helical buckling of a non-Brownian filament. Typical buckling sequence in a simulation of a non-Brownian filament with $\bar{\mu} = 6.5 \times 10^4$. In the simulation shown, deformations first occur in a 2D plane before the 3D helical shape develops. Deformations also tend to be largest near the centre of the filament. See also Supplementary Video 8.

of buckling and subsequent mode shapes^{6,7,10,29}. Here, we show how the interaction of pairs of planar eigenmodes growing in different planes is responsible for the observed 3D helices.

In the absence of thermal fluctuations, filament dynamics are governed by the interplay of viscous forces exerted by the flow and internal elasticity. This balance is quantified by $\bar{\mu}$, comparing the characteristic timescale for elastic relaxation of a bending mode with the timescale of the imposed flow¹⁴. It is defined as $\bar{\mu} = 8\pi\mu\dot{e}L^4/Bc$ in terms of the solvent viscosity μ , \dot{e} , filament contour length L and bending rigidity B and shows a strong dependence on length. The constant $c = -\ln(\alpha^2 e)$ is a dimensionless slenderness parameter where α is the filament aspect ratio and e is Euler's number. When the filament is small enough to experience Brownian motion, the balance of fluctuations and bending rigidity results in a persistence length $\ell_p = B/k_B T$, where $k_B T$ is the thermal energy. In this case, the ratio ℓ_p/L quantifies the amplitude of fluctuations, with the limit of $\ell_p/L \rightarrow \infty$ describing Brownian rigid fibres. In past studies of viscous buckling, the role of thermal fluctuations was shown to be limited to triggering the instability while smoothing the buckling transition^{8,14,29}. We neglect fluctuations in our theory, though their effect will be addressed in simulations.

In the reference frame of the translating filament, the local flow field is well approximated by a planar compressional flow in experiments and Brownian simulations, and by a uniaxial compressional flow in non-Brownian simulations; we focus here on the former case and thus take the dimensionless flow field to be $\mathbf{u}_\infty = (-x, y, 0)$. In the base state, the filament is straight with its centre at the stagnation point and its axis aligned with the direction of compression: $\mathbf{x}_0(s) = s\hat{\mathbf{x}}$ with $s \in [-0.5, 0.5]$. Its motion is described using local slender-body theory for low-Reynolds-number hydrodynamics³²,

$$\bar{\mu} (\dot{\mathbf{x}} - \mathbf{u}_\infty) = (\mathbb{I} + \mathbf{x}_s \mathbf{x}_s) \cdot [(T \mathbf{x}_s)_s - \mathbf{x}_{ssss}] \quad (1)$$

where $\bar{\mu}$ appears as the sole control parameter. Here, we have assumed a high aspect ratio ($c \gg 1$), and in this limit the friction coefficients in the parallel and perpendicular directions differ by a factor of 1/2. Indices in equation (1) denote differentiation with respect to arclength, with \mathbf{x}_s describing the local tangent vector. The scalar $T(s)$ is the internal tension that enforces filament inextensibility. Equation (1) is accompanied by force- and moment-free boundary conditions: $\mathbf{x}_{sss} = \mathbf{x}_{ss} = T = 0$ at $s = \pm 1/2$. In the base state, the compressional flow induces a parabolic tension profile $T_0(s) = \frac{1}{4}\bar{\mu}(s^2 - \frac{1}{4})$ typical of undeformed filaments in linear flows^{6,7}.

The straight configuration is perturbed as $\mathbf{x}(s, t) = (s, h_y, h_z)$, where $h_y(s, t)$ and $h_z(s, t)$ are in-plane (x, y) and out-of-plane (x, z) shape perturbations, respectively, and are assumed to be small $\mathcal{O}(\epsilon)$ quantities. We first perform a linear analysis and simplify equation (1) as

$$\bar{\mu} (\dot{\mathbf{x}} - \mathbf{u}_\infty) = T_0 \mathbf{x}_{ss} + 2T_{0,s} \mathbf{x}_s - \mathbf{x}_{ssss} + \mathcal{O}(\epsilon^2) \quad (2)$$

where $\mathbf{u}_\infty = (-s, h_y, 0)$. We seek normal-mode perturbations of the form $\{h_y, h_z\} = \{\Phi_y(s), \Phi_z(s)\} \exp(i\sigma t)$, where Φ_y and Φ_z are

in- and out-of-plane mode shapes and σ is the complex growth rate. Inserting this ansatz into equation (2) yields two eigenvalue problems in the y and z directions:

$$\bar{\mu}(\sigma - 1) \Phi_y = \mathcal{L}[\Phi_y] \quad (3)$$

$$\bar{\mu}\sigma \Phi_z = \mathcal{L}[\Phi_z] \quad (4)$$

where \mathcal{L} is the differential operator $\mathcal{L}[\Phi] = T_0(s)\Phi_{ss} + T_{0,s}(s)\Phi_s - \Phi_{ssss}$. Inspection of equations (3) and (4) shows that the eigenvalue problems in the two orthogonal planes are uncoupled and thus have their own growth rates (σ_y, σ_z). Incidentally, the two eigenvalue problems are found to be identical under the transformation $\sigma_z = \sigma_y - 1$. This points to a key aspect of the eigenspectrum: for a given value of $\bar{\mu}$, in- and out-of-plane mode shapes are identical but have offset growth rates. The reason that the two eigenvalues are nearly identical is the internal tension, which acts to destabilize the system equally in all directions. Out-of-plane deformations grow slightly more slowly as a consequence of the 2D nature of the flow; the two growth rates would be identical in uniaxial flow.

The eigenvalue problem of equation (3) was solved numerically using a Chebyshev spectral collocation method with boundary conditions $\Phi_{yss} = \Phi_{ysss} = 0$ at $s = \pm 1/2$, and pertinent results are summarized in Fig. 3. The growth rates $\text{Re}(\sigma_y)$ of unstable modes are plotted versus $\bar{\mu}$ in Fig. 3a. In very weak flows, all modes are stable with negative growth rates. As the elastoviscous number is increased, a supercritical pitchfork bifurcation occurs, giving rise to the first onset of buckling. In agreement with past planar analyses^{7,29,30}, the first buckling threshold is found to be $\bar{\mu}_c \approx 153.2$ with an even mode shape ($\Phi(-s) = \Phi(s)$) resembling the canonical C shape typical of Euler buckling. At yet larger values of $\bar{\mu}$, higher-order buckling modes with larger wavenumbers are excited and can become unstable, leading to the complex eigenspectrum of Fig. 3a. Three essential features stand out: (1) at large elastoviscous numbers, the first two eigenvalues $\{\sigma_y^{(1)}, \sigma_y^{(2)}\}$ dominate the spectrum and the corresponding eigenmodes are expected to dictate the emergent morphologies; (2) these two dominant eigenmodes always come in an odd–even pair, that is, if $\Phi^{(1)}$ is odd then $\Phi^{(2)}$ is even and vice versa; (3) the difference in growth rate between these two dominant modes becomes negligible in strong flows. This last point is made clear in the inset of Fig. 3a, where the difference $\Delta\sigma$ between the two growth rates is seen to decay rapidly with $\bar{\mu}$.

We are now in a position to explain the emergence of helicoidal shapes. In a strong flow, unstable eigenmodes are planar but can develop and grow in any plane containing the flow axis. In addition, dominant modes always come in odd–even pairs with nearly identical growth rates. When a straight filament is perturbed, there is thus a strong likelihood for the two modes to grow simultaneously. The superposition of two adjacent odd–even planar modes such as those shown in Fig. 3b growing in different planes produces a coiled 3D conformation that resembles a helix and continues to grow as such, with the two modes interacting as a consequence of geometric nonlinearities. A similar mechanism was previously proposed to explain the buckling of elastic rods in soft elastomer matrices³³, though the governing equations and forces at play are very different in that problem.

The process by which linear buckling modes interact to produce helices can be formalized by deriving a nonlinear amplitude equation of the Ginzburg–Landau form³⁴, as we briefly outline (see Supplementary Information for details). Close to the onset of buckling, we expand deformations on the basis of the first two linear eigenmodes as they dominate the unstable spectrum: $h_{yz}(s, t) = A_1^{yz}(t)\Phi^{(1)}(s) + A_2^{yz}(t)\Phi^{(2)}(s)$. We emphasize that the bases used for the expansion in the two orthogonal planes are the

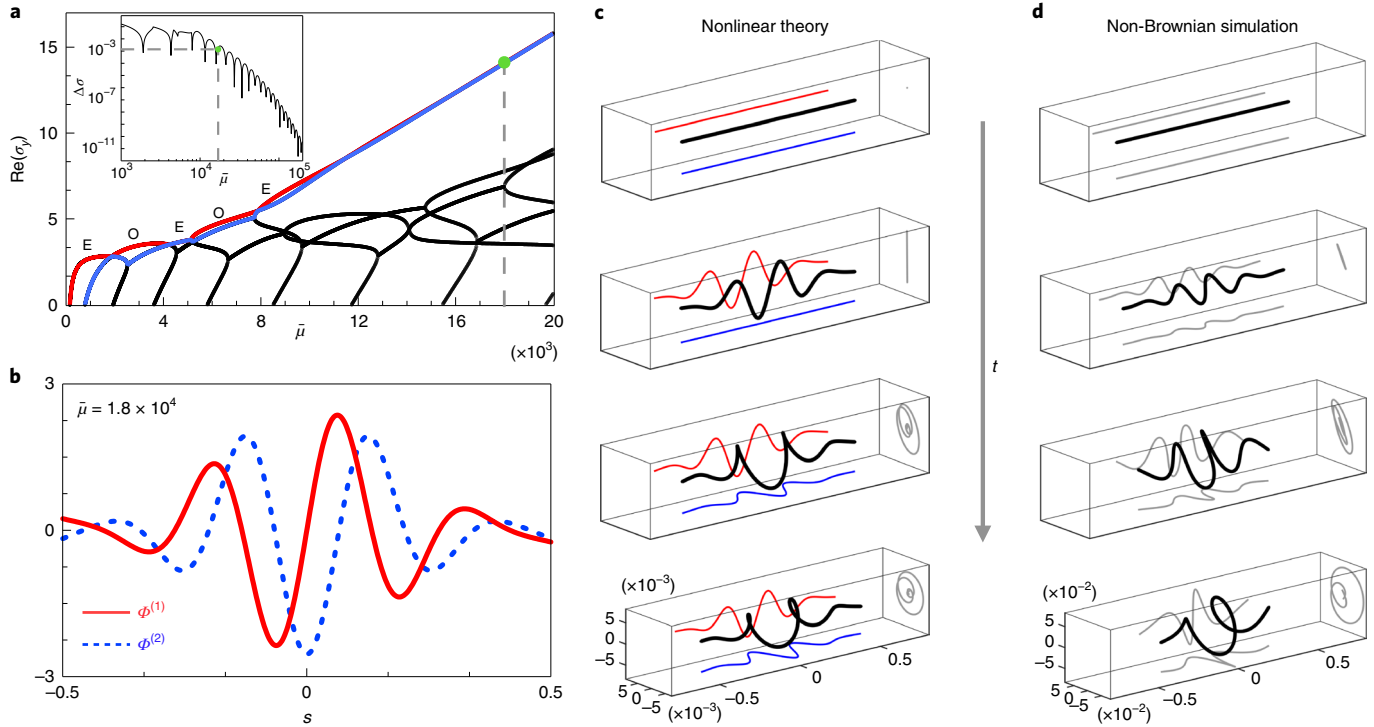


Fig. 3 | Stability analysis and rationale for helical shapes. **a**, Growth rates of unstable planar eigenmodes plotted versus elastoviscous number. As $\bar{\mu}$ increases, additional modes become unstable. The two dominant eigenvalues are coloured in red and blue and labelled as either even (E) or odd (O) functions of s . Inset: difference $\Delta\sigma$ between the two most unstable eigenvalues as a function of $\bar{\mu}$, showing convergence in strong flows. **b**, Eigenmodes associated with the two largest eigenvalues for a value of $\bar{\mu} = 1.8 \times 10^4$ corresponding to the green dot in **a**. The dominant mode $\Phi^{(1)}$ is odd, whereas $\Phi^{(2)}$ is even. **c**, Snapshots from a time sequence predicted by the nonlinear model, showing the formation of a 3D coiled conformation from the superposition of adjacent even and odd planar eigenmodes in orthogonal planes. See Supplementary Video 9 for an animation. **d**, Buckling sequence in a non-Brownian simulation at the same value of $\bar{\mu}$, also showing the growth of a helix from an initially planar buckling mode. See also Supplementary Video 7.

same, since the unstable mode shapes arising from the linear stability are identical, as seen from equations (3) and (4). Retaining nonlinear terms in equation (1) and using the orthogonality of the linear eigenfunctions with the eigenfunctions of the adjoint linear operator provides a system of coupled nonlinear ordinary differential equations for the four unknown time-dependent amplitudes. Solutions of this system exhibit amplitude saturation following an initial exponential growth regime, and in sufficiently strong flows always produce 3D helical conformations consistent with observations. Remarkably, even planar initial conditions evolve towards helical shapes as nonlinearities force the modes to interact and spontaneously break symmetry. This mechanism is illustrated in Fig. 3b,c for a representative $\bar{\mu} = 1.8 \times 10^4$ (see also Supplementary Video 9). The two dominant linear eigenmodes in this case are plotted in Fig. 3b, where $\Phi^{(1)}$ is found to be odd while $\Phi^{(2)}$ is even. A superposition of these modes in orthogonal planes does indeed produce a helix in Fig. 3c, showing snapshots from a numerical solution of the weakly nonlinear model in which the spontaneous symmetry breaking is evident. We note that helix formation is also supported by a favourable energetic landscape (see Supplementary Fig. 8): a filament that is forcefully restricted to buckle and compress in two dimensions does indeed show a monotonic growth of its bending energy that is avoided by the provision to coil²⁸.

The mechanism by which planar modes interact to create coiled morphologies is corroborated by non-Brownian simulations at the same value of $\bar{\mu}$ in Fig. 3d: in this example, the helical morphology is also seen to emerge from an initially planar buckling mode and has a final shape that resembles the theoretical prediction of Fig. 3c.

The mechanism is also consistent with the findings of Fig. 1, where we observed that helical buckling only occurs at large $\bar{\mu}$: in weak flows, the two dominant eigenvalues are well separated, resulting in the exponential growth of a single dominant mode and emergence of a planar shape. While we anticipate that planar buckling may also occur in experiments and Brownian simulations, it is typically not observed, as thermal shape fluctuations immediately promote a 3D shape.

The radius of the helix is independent of filament length

We now quantify the evolution of the shape during a buckling event from experiments and simulations. Fig. 4a shows the helix length, estimated as the end-to-end distance L_{ee} , and effective radius R as functions of dimensionless time from an experimental realization; similar observations are made in simulations (see Supplementary Fig. 4). In all cases, L_{ee} decreases and R increases as the helix forms and is compressed by the flow. The nearly linear decrease of L_{ee} with time allows us to extract a characteristic speed $|L_{ee}|$ for compression of the helix, which we plot as a function of $\dot{\epsilon}L$ in Fig. 4b. A linear relationship $|L_{ee}| \sim 0.7\dot{\epsilon}L$ is found in both experiments and simulations, with a slope of less than unity that we attribute to the finite elastic resistance of the buckled helical shapes.

In the final stage of compression, the growth of the helix radius slows down as seen in Fig. 4a, and a nearly steady shape is reached with a roughly constant radius. We measure this final coiling radius from experiments and corresponding simulations (see Methods and Supplementary Information for details) and discuss its dependence on the relevant parameters. Experiments typically have access

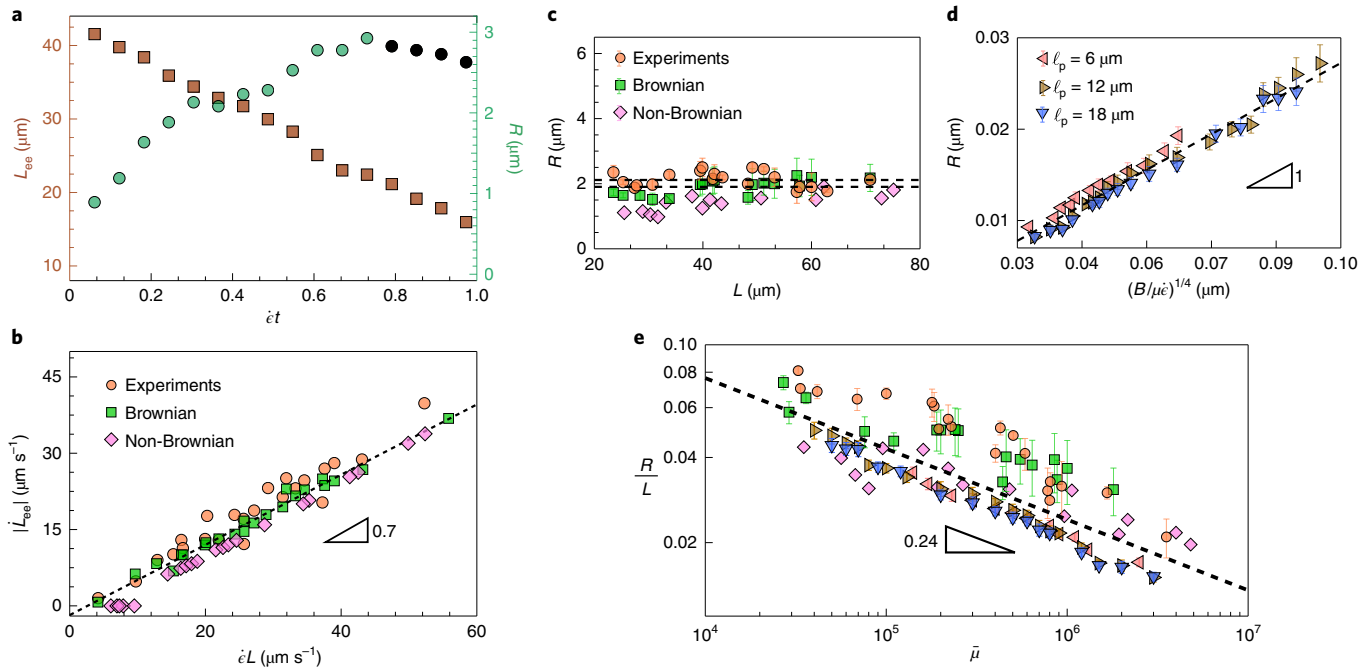


Fig. 4 | Temporal dynamics and final helix radius. **a**, Evolution of L_{ee} and R as functions of $\dot{\epsilon}t$ in an experiment with $L = 42.1\mu\text{m}$ and $\dot{\epsilon} = 0.61\text{s}^{-1}$ (see Supplementary Fig. 4 for corresponding data from simulations). The range used to estimate the final helix radius is shown in black. **b**, Compression speed of the helix estimated as the rate of change of the end-to-end distance, showing a linear dependence on $\dot{\epsilon}L$ with a slope of ~ 0.7 . **c**, Final dimensional radius as a function of contour length in experiments and both types of simulation, for strain rates in the range $\dot{\epsilon} \sim 0.3\text{--}0.61\text{s}^{-1}$. The two dashed lines show the mean radius for experiments (top) and Brownian simulations (bottom), which differ slightly due to the two different methods for estimating R . **d**, Final R as a function of $(B/\mu\dot{\epsilon})^{1/4}$ in Brownian simulations for varying l_p , showing a linear dependence in agreement with equation (5). In these simulations, $L = 0.6\mu\text{m}$ and $\dot{\epsilon} \sim 10^5\text{--}10^7\text{s}^{-1}$. See also Supplementary Video 6. **e**, Collapse of all the data from experiments, Brownian and non-Brownian simulations when plotted in dimensionless variables, showing a power-law scaling of the form $R/L \sim \bar{\mu}^{-0.24}$. Error bars in **c**–**e** show 1 s.d. over the averaging window defined in **a**.

to a limited range of strain rates ($\sim 0.4\text{--}0.6\text{s}^{-1}$), so variations in $\bar{\mu}$, covering over three decades, are primarily due to variations in L . Consequently, the radius is first displayed in Fig. 4c as a function of L , keeping all other parameters constant. Quite surprisingly, a nearly constant value of R is observed, indicating that the final helix radius is largely independent of contour length. The agreement between experiments and simulations for the same conditions is again very good.

This peculiar result can be rationalized by a scaling theory for the radius of an inextensible helix undergoing compression in flow (see Supplementary Information for details). During compression, the pitch of the helix decreases, causing its radius to increase by inextensibility. Balancing the associated viscous dissipation with the rate of change of elastic bending energy during this process yields the simple scaling

$$R \sim \left(\frac{B}{\mu\dot{\epsilon}} \right)^{1/4} \quad (5)$$

which is indeed independent of contour length and only weakly dependent on compression rate. This result points to the elasto-viscous length $(B/\mu\dot{\epsilon})^{1/4}$ (ref. 35), which is the only length scale of the problem besides L , as the fundamental scale for the buckling process. To test this scaling law and probe the dependence on flow strength and bending rigidity, we performed additional Brownian simulations in which strain rate and persistence length were varied while keeping L constant. The measured radius for three different persistence lengths is displayed in Fig. 4d as a function of the elasto-viscous length and shows a clear collapse of the data, corroborating the scaling prediction. Finally, we summarize all the data from

experiments and both types of simulation in dimensionless form in Fig. 4c, where our model predicts

$$\frac{R}{L} \sim \bar{\mu}^{-1/4} \quad (6)$$

A similar collapse is found, with some scatter arising from fluctuation-induced defects. A numerical fit yields an exponent of -0.24 , in excellent agreement with the scaling prediction.

A generic transition in strain-dominated flows

We have elucidated the coiled morphologies of actin filaments in compressional flow through a combination of experiments, simulations, scaling analysis and weakly nonlinear stability theory. The two distinct approaches used in numerical simulations highlight the robustness of this phenomenon, in which neither Brownian fluctuations nor a 3D flow field are necessary conditions for helical buckling. The stability theory also supports this idea and explains the origin of these structures in a simple 2D stagnation point flow. As uncovered in our analysis, the key to helical coiling is the nature of the eigenspectrum associated with the linearized buckling problem, in which dominant eigenmodes come in odd–even pairs with nearly identical growth rates and interact nonlinearly to form helicoidal shapes. Our analysis is an addition to the study of post-buckling mode interactions that are often responsible for non-planar structures³⁶. Remarkably, this distribution of eigenvalues is quite generic, and helical buckling has also recently been observed for very flexible filaments in shear flow (see Supplementary Fig. 10), where the dynamics is more subtle due to the non-stationary base state of a tumbling straight filament.

The helical buckling instability uncovered here probably serves as an explanation for a number of past experimental observations where helicoidal morphologies were reported but largely overlooked: for example, during the manufacturing of synthetic wet-spun fibres for cosmetics, where long fibres undergo buckling in a compressional flow³⁷, in biology, where the sessile protozoan *Vorticella* is known to propel by exploiting the sudden calcium-powered contraction of its slender stalk³⁸, or during the transport of elastic fibres in turbulent flows³⁹. The fundamental mechanism highlighted by our analysis should advance our understanding of these various phenomena and may also be exploited for the controlled microfabrication of chiral objects from 1D elastic filaments.

Online content

Any methods, additional references, Nature Research reporting summaries, source data, extended data, supplementary information, acknowledgements, peer review information; details of author contributions and competing interests; and statements of data and code availability are available at <https://doi.org/10.1038/s41567-020-0843-7>.

Received: 10 September 2019; Accepted: 14 February 2020;

Published online: 30 March 2020

References

- Lauga, E. Bacterial hydrodynamics. *Annu. Rev. Fluid Mech.* **48**, 105–130 (2016).
- Abkarian, M. & Viallat, A. in *Fluid-Structure Interactions in Low-Reynolds-Number Flows* (eds Duprat, C. & Stone, H.) 347–362 (Royal Society of Chemistry, 2015).
- Nazockdast, E., Rahimian, A., Needleman, D. & Shelley, M. J. Cytoplasmic flows as signatures for the mechanics of mitotic positioning. *Mol. Biol. Cell* **28**, 3261–3270 (2016).
- Chen, D., Yoon, J., Chandra, D., Crosby, A. J. & Hayward, R. C. Stimuli-responsive buckling mechanics of polymer films. *J. Polym. Sci. B* **52**, 1441–1461 (2014).
- du Roure, O., Lindner, A., Nazockdast, E. N. & Shelley, M. J. Dynamics of flexible fibers in viscous flows and fluids. *Annu. Rev. Fluid Mech.* **51**, 539–572 (2019).
- Becker, L. E. & Shelley, M. J. Instability of elastic filaments in shear flow yields first-normal-stress differences. *Phys. Rev. Lett.* **87**, 198301 (2001).
- Young, Y.-N. & Shelley, M. J. Stretch-coil transition and transport of fibers in cellular flows. *Phys. Rev. Lett.* **99**, 058303 (2007).
- Kantsler, V. & Goldstein, R. E. Fluctuations, dynamics, and the stretch-coil transition of single actin filaments in extensional flows. *Phys. Rev. Lett.* **108**, 038103 (2012).
- Guglielmini, L., Kushwaha, A., Shaqfeh, E. S. G. & Stone, H. A. Buckling transitions of an elastic filament in a viscous stagnation point flow. *Phys. Fluids* **24**, 123601 (2012).
- Lindner, A. & Shelley, M. in *Fluid-Structure Interactions in Low-Reynolds-Number Flows* (eds Duprat, C. & Stone, H.) 168–192 (Royal Society of Chemistry, 2015).
- Li, L., Manikantan, H., Saintillan, D. & Spagnolie, S. The sedimentation of flexible filaments. *J. Fluid Mech.* **735**, 705–736 (2013).
- Forgacs, O. L. & Mason, S. G. Particle motions in sheared suspensions: X. Orbita of flexible threadlike particles. *J. Colloid Sci.* **14**, 473–491 (1959).
- Harasim, M., Wunderlich, B., Peleg, O., Kröger, M. & Bausch, A. R. Direct observation of the dynamics of semiflexible polymers in shear flow. *Phys. Rev. Lett.* **110**, 108302 (2013).
- Liu, Y., Chakrabarti, B., Saintillan, D., Lindner, A. & du Roure, O. Morphological transitions of elastic filaments in shear flow. *Proc. Natl Acad. Sci. USA* **115**, 9438–9443 (2018).
- Nguyen, H. & Fauci, L. Hydrodynamics of diatom chains and semiflexible fibres. *J. R. Soc. Interface* **11**, 20140314 (2014).
- LaGrone, J., Cortez, R., Yan, W. & Fauci, L. Complex dynamics of long, flexible fibers in shear. *J. Non-Newtonian Fluid Mech.* **269**, 73–81 (2019).
- Kuei, S., Słowińska, A. M., Ekiel-Jeżewska, M. L., Wajnryb, E. & Stone, H. A. Dynamics and topology of a flexible chain: knots in steady shear flow. *New J. Phys.* **17**, 053009 (2015).
- Silverberg, J. L. et al. 3D imaging and mechanical modeling of helical buckling in *Medicago truncatula* plant roots. *Proc. Natl Acad. Sci. USA* **109**, 16794–16799 (2012).
- Svenské, D. & Podgornik, R. Confined nanorods: jamming due to helical buckling. *Phys. Rev. E* **77**, 031808 (2008).
- Klug, W. S., Feldmann, M. T. & Ortiz, M. Three-dimensional director-field predictions of viral DNA packing arrangements. *Comput. Mech.* **35**, 146–152 (2005).
- Miller, J. T. et al. Buckling of a thin elastic rod inside a horizontal cylindrical constraint. *Extreme Mech. Lett.* **3**, 36–44 (2015).
- Goriely, A. & Tabor, M. The nonlinear dynamics of filaments. *Nonlinear Dyn.* **21**, 101–133 (2000).
- Van der Heijden, G. H. M. & Thompson, J. M. T. Helical and localised buckling in twisted rods: a unified analysis of the symmetric case. *Nonlinear Dyn.* **21**, 71–99 (2000).
- Antman, S. S. *Nonlinear Problems of Elasticity* (Springer, 2005).
- Zografas, K., Pimenta, F., Alves, M. A. & Oliveira, M. S. N. Microfluidic converging/diverging channels optimised for homogeneous extensional deformation. *Biomicrofluidics* **10**, 043508 (2016).
- Liu, Y. *Dynamics of Flexible and Brownian Filaments in Viscous Flow*. Ph.D. thesis, Univ. Sorbonne Paris Cité (2018).
- LaGrone, J., Cortez, R. & Fauci, L. Elastohydrodynamics of swimming helices: effects of flexibility and confinement. *Phys. Rev. Fluids* **4**, 033102 (2019).
- Chelakkot, R., Winkler, R. G. & Gompper, G. Flow-induced helical coiling of semiflexible polymers in structured microchannels. *Phys. Rev. Lett.* **109**, 178101 (2012).
- Manikantan, H. & Saintillan, D. Buckling transition of a semiflexible filament in extensional flow. *Phys. Rev. E* **92**, 041002 (2015).
- Quennouz, N., Shelley, M., du Roure, O. & Lindner, A. Transport and buckling dynamics of an elastic fibre in a viscous cellular flow. *J. Fluid Mech.* **769**, 387–402 (2015).
- Goriely, A. & Tabor, M. Spontaneous helix hand reversal and tendril perversions in climbing plants. *Phys. Rev. Lett.* **80**, 1564–1567 (1998).
- Batchelor, G. K. Slender-body theory for particles of arbitrary cross-section in Stokes flow. *J. Fluid Mech.* **44**, 419–440 (1970).
- Su, T., Liu, J., Terwagne, D., Reis, P. M. & Bertoldi, K. Buckling of an elastic rod embedded on an elastomeric matrix: planar vs. non-planar configurations. *Soft Matter* **10**, 6294–6302 (2014).
- Drazin, P. G. & Reid, W. H. *Hydrodynamic Stability* (Cambridge Univ. Press, 2004).
- Coq, N., du Roure, O., Marthelot, J., Bartolo, D. & Fermigier, M. Rotational dynamics of a soft filament: wrapping transition and propulsive forces. *Phys. Fluids* **20**, 051703 (2008).
- Byskov, E. & Hutchinson, W. Mode interaction in axially stiffened cylindrical shells. *AIAA J.* **15**, 941–948 (1977).
- Mercader, C. et al. Kinetics of fiber solidification. *Proc. Natl Acad. Sci. USA* **107**, 18331–18335 (2010).
- Ryu, S., Pepper, R. E., Nagai, M. & France, D. C. *Vorticella*: a protozoan for bio-inspired engineering. *Micromachines* **8**, 4 (2016).
- Allende, S., Henry, C. & Bec, J. Stretching and buckling of small elastic fibers in turbulence. *Phys. Rev. Lett.* **121**, 154001 (2018).

Publisher's note Springer Nature remains neutral with regard to jurisdictional claims in published maps and institutional affiliations.

© The Author(s), under exclusive licence to Springer Nature Limited 2020

Methods

Experiments. The protocol for the assembly of actin filaments is well controlled and reproducible. Concentrated G-actin, which is obtained from rabbit muscle cells and purified according to the protocol described in refs. ^{14,40}, is placed in F-buffer (10-mM Tris-HCl, pH = 7.8, 0.2-mM ATP, 0.2-mM CaCl₂, 1-mM DTT, 1-mM MgCl₂, 100-mM KCl, 0.2-mM EGTA and 0.145-mM 1,4-diazabicyclo[2.2.2]octane) at a concentration of 1 μM. At the same time, Alexa488 fluorescent phalloidin at the same molarity as G-actin is added to stabilize and visualize actin filaments. After 1 h of polymerization in the dark at room temperature, concentrated F-actin is diluted 20- to 50-fold for the following experiments. 45.5 % (w/v) sucrose is added to match the refractive index of the poly(dimethylsiloxane) channel ($n = 1.41$) to obtain better image contrast. The viscosity of the suspending fluid with 45.5 % (w/v) sucrose is 5.6 mPa s at 24 °C, measured with an Anton Paar MCR 501 rheometer. The filaments obtained with this protocol have $\ell_p = 17 \pm 1 \mu\text{m}$ and $L \sim 20\text{--}80 \mu\text{m}$.

A hyperbolic poly(dimethylsiloxane) channel, which has been optimized by taking into account the effect of the varying rectangular cross-section²⁵, is used to provide the background straining flow. In this geometry, filaments experience homogeneous strain rates for a certain residence time as they are transported in the centre of the channel by a flow-focusing mechanism. An automated tracking system is used to keep filaments in the visual field of the camera, with an image blur of $\lesssim \pm 0.5 \mu\text{m}$ due to velocity differences between stage and flow. A stable flow is driven by a syringe pump (neMESYS 290N) and particle tracking velocimetry is used to ensure that the velocity profile is in agreement with theoretical predictions³⁶. The lengths of the channel sections with constant strain rate and linearly varying strain rate are 1,200 μm and 800 μm, respectively, with a channel width of 789 μm upstream and 107 μm at the centre. The channel has a uniform depth of 100 μm in the z direction. The total flow rate Q is in the range of 3.1–5.5 nL s⁻¹, which provides average velocities of $\sim 100 \mu\text{m s}^{-1}$, maximum velocities of $\sim 1 \text{ mm s}^{-1}$ and a range of compression rates $\dot{\epsilon} \sim 0.4\text{--}0.6 \text{ s}^{-1}$.

Images are captured using a complementary metal–oxide–semiconductor camera (Hamamatsu Orca flash 4.0LT, 16 bits) with an exposure time $\Delta t = 40 \text{ ms}$, and are synchronized with the stage displacements through external triggers. The shapes of the actin filaments are extracted through Gaussian blur, threshold, noise reduction and skeletonize procedures in the software ImageJ. A customized MATLAB code based on B-spline interpolation is then used to reconstruct the filament centreline along s and to calculate relevant parameters.

Numerical simulations. We have performed two complementary sets of simulations in two different flow geometries. Full details of the simulation methods are provided in Supplementary Information. In the Brownian simulations, the filaments are modelled as inextensible Euler–Bernoulli beams, and their dynamics in flow are captured using local slender-body theory, which accounts for drag anisotropy⁴¹. Brownian fluctuations are included and calculated to satisfy the fluctuation–dissipation theorem^{14,42}. The background flow is chosen to be a purely 2D compressional flow in free space, with $\mathbf{u}_\infty = (-x, y, 0)$. The chosen background velocity field is an approximation to the experimental flow field measured in the channel mid-plane, where measurements are performed²⁶. We use a straight initial condition for the filaments to emulate the hydrodynamic stretching taking place in the convergent part of the channel in the experiments.

In the non-Brownian simulations, the fibres are modelled as a network of Hookean springs that provide structural rigidity to the filaments¹⁵, with hydrodynamics captured by the method of regularized Stokeslets⁴³. The filaments are finitely extensible and approach the limit of inextensibility for very small aspect ratio. We performed these simulations in an axisymmetric channel of circular cross-section that provides regions of constant compression and extension as in the experiments¹⁶.

Shape characterization. We track the evolution of the helix shape as a function of Hencky strain $\dot{\epsilon}t$, which is a measure of the accumulated strain experienced by the filaments from $t = 0$, when their centre of mass enters the compressional region. The length is simply estimated using $L_{\text{co}}(t) = \|\mathbf{x}(L, t) - \mathbf{x}(0, t)\|$ in the plane of motion, where $\mathbf{x}(s, t)$ is a Lagrangian parameterization of the filament centreline with $s \in [0, L]$. Estimating the coil radius is more challenging and is done using two complementary approaches illustrated in Supplementary Fig. 3. As experiments only provide shape projections in the (x, y) plane, we estimate the radius in terms

of the lateral extent of the filament as $R_\perp(t) = [y_{\max}(t) - y_{\min}(t)]/2$. In simulations, the full filament shape is available and we define an effective radius by fitting the cross-sectional projection in the (y, z) plane with a circle: $R_{\text{eff}}(t) = \langle y(s, t)^2 + z(s, t)^2 \rangle_s$. In both cases, we only consider the central part of the filament, where the conformation is mostly helical, and omit filament ends.

In experiments and Brownian simulations, the final helix shape is reached near a Hencky strain of unity, and we estimate the final radius by averaging either $R_\perp(t)$ or $R_{\text{eff}}(t)$ over $\dot{\epsilon}t \sim 0.8\text{--}1$. In non-Brownian simulations, filaments typically experience larger Hencky strains, though the key features of the dynamics remain unaltered; in this case, we estimate the final radius by performing the average over $\dot{\epsilon}t \sim 1.6\text{--}2$.

Data availability

Source data for Figs. 1, 3 and 4 are provided with the paper. All other data that support the plots within this paper and other findings of this study are available from the corresponding authors upon reasonable request.

Code availability

The numerical codes used for the stability analysis and for simulations are available from the corresponding authors upon reasonable request.

References

40. Spudich, J. A. & Watt, S. The regulation of rabbit skeletal muscle contraction. I. Biochemical studies of the interaction of the tropomyosin-troponin complex with actin and the proteolytic fragments of myosin. *J. Biol. Chem.* **246**, 4866–4871 (1971).
41. Tornberg, A.-K. & Shelley, M. J. Simulating the dynamics and interactions of flexible fibers in Stokes flows. *J. Comput. Phys.* **196**, 8–40 (2004).
42. Manikantan, H. & Saintillan, D. Subdiffusive transport of fluctuating elastic filaments in cellular flows. *Phys. Fluids* **25**, 073603 (2013).
43. Cortez, R., Fauci, L. & Medovikov, A. The method of regularized Stokeslets in three dimensions: analysis, validation, and application to helical swimming. *Phys. Fluids* **17**, 031504 (2005).

Acknowledgements

We thank R. Winkler for helping us appreciate the prevalence of helical shapes, as well as M. Shelley and E. Shafqeh for illuminating discussions. We are grateful to G. Romet-Lemonne and A. Jégou for providing purified actin and to T. Darnige for help with the programming of the microscope stage. We also thank M. Oliveira and J. Fidalgo for help with the implementation of the optimized hyperbolic microchannel and filament tracking. A.L., B.C. and Y.L. acknowledge funding from the ERC Consolidator Grant PaDyFlow (Agreement 682367). D.S. acknowledges funding from a Paris Sciences Chair from ESPCI Paris. This work received the support of Institut Pierre-Gilles de Gennes (Équipement d’Excellence, ‘Investissements d’Avenir’, programme ANR-10-EQPX-34). J.L., R.C. and L.F. acknowledge funding from a Gulf of Mexico Research Initiative grant and from National Science Foundation grant no. DMS-1043626.

Author contributions

B.C. and D.S. performed the Brownian simulations, stability analysis and scaling theory. Y.L., O.d.R. and A.L. performed experiments. J.L., R.C. and L.F. performed non-Brownian simulations. All authors contributed to the analysis and interpretation of data and to the preparation of figures. B.C., D.S., A.L., O.d.R., Y.L. and L.F. wrote the paper.

Competing interests

The authors declare no competing interests.

Additional information

Supplementary information is available for this paper at <https://doi.org/10.1038/s41567-020-0843-7>.

Correspondence and requests for materials should be addressed to Y.L. or D.S.

Reprints and permissions information is available at www.nature.com/reprints.